MDPI

Article

The Evolution of Abnormal Grains during the Heating Stage of a Post-Weld Solution Treatment in a Friction-Stir-Welded 2519 Aluminium Alloy

Ivan S. Zuiko [1], Sergey Malopheyev [1], Salaheddin Rahimi [2], Sergey Mironov [1,*] and Rustam Kaibyshev [1]

[1] Laboratory of Mechanical Properties of Nanoscale Materials and Superalloys, Belgorod National Research University, Pobeda 85, 308015 Belgorod, Russia; zuiko_ivan@bsu.edu.ru (I.S.Z.); malofeev@bsu.edu.ru (S.M.); rustam_kaibyshev@bsu.edu.ru (R.K.)

[2] Advanced Forming Research Centre, University of Strathclyde, 85 Inchinnan Drive, Glasgow PA4 9LJ, UK; salah.rahimi@strath.ac.uk

* Correspondence: mironov@bsu.edu.ru; Tel.: +7-4722-585456

Abstract: This work presents an in-depth investigation of the early stages of abnormal grain growth (AGG) in a friction-stir-welded (FSWed) 2519-T820 aluminium alloy. Microstructural evolutions, which occurred during the heating stage of a solution heat treatment (SHT), were studied. It was found that the welded materials underwent a complex sequence of precipitation phenomena, which eventually led to AGG. The evolution of precipitates was found to be heavily dependent on the FSW temperature condition. In a weld produced with a low-heat input, a significant portion of the precipitates were retained in the stir zone after FSW and then underwent coarsening and a subsequent dissolution during the annealing that followed. This led to a reduction in precipitation-pinning forces and thus promoted rapid grain coarsening. In a weld produced with a high-heat input, the initial precipitates were completely dissolved during the FSW, owing to the higher temperature, and then partially re-precipitated during the heating stage of the post-weld heat treatment. Due to the fine-grain structure of the stir zone, re-precipitation typically occurred at grain boundaries, thus promoting significant thermal stability. However, at temperatures approaching the SHT temperature, the new precipitates coarsened and then dissolved, resulting in AGG.

Keywords: abnormal grain growth (AGG); microstructure; aluminium alloys; friction-stir welding (FSW); secondary precipitates

1. Introduction

Heat-treatable aluminium alloys are of great interest for various structural applications due to their excellent combination of good formability, corrosion resistance, low density, and superior strength. However, for a long time, poor weldability has been commonly recognized as an intrinsic drawback for these materials. The invention of the friction-stir welding (FSW) technique in the 1990s led to a major breakthrough in overcoming this problem [1]. Owing to its solid-state nature, FSW eliminates solidification defects, such as voids and cracks, and thus routinely produces sound joints in most aluminium alloys. This has created new opportunities for manufacturing more complex components from these alloys for various industrial applications, e.g., [2–4]. Specifically, FSW has been successfully deployed as an alternative to conventional fusion welding or riveting for the manufacturing of large-scale structures, such as aircraft fuselage skins, train cars, etc., in the transportation industry.

However, the technology still needs modifications to achieve the desired microstructures for tailored mechanical properties. Despite being a solid-state welding technique, during FSW the temperature typically exceeds 0.5 T_m (where T_m is the melting point of the material). This consequently leads to the dissolution and/or coarsening of the constituent second-phase precipitates in the weld zone, resulting in a soft material (e.g., [5,6]). To

achieve a material with the desired strength, the welds must be subjected to appropriate heat treatments, which sometimes involve solution annealing and subsequent artificial ageing. This has frequently been seen to lead to abnormal grain growth (AGG) in the stir zone, a phenomenon involving a significant coarsening of some grains, which tend to consume a considerable portion of the microstructure [7–37]. This undesirable phenomenon has been reported for almost all heat-treatable aluminium alloys, including the 2xxx [7–16], 6xxx [17–22], and 7xxx [11,24–32] series as well as their dissimilar combinations [30–37] that show similar characteristics.

Specifically, Liu et al. [7,10] have observed the AGG in the 2219-T6 aluminium alloy. It was concluded that this undesirable phenomenon reduced the superplastic ductility of friction-stir-processed materials at elevated temperatures [7]. Attallah et al. [8] revealed the catastrophic microstructural coarsening in the 2095 aluminium alloy. Moreover, it was found that a decrease in the FSW heat input tended to degrade the thermal stability of the welded material. The same effect has been established by Kalinenko et al. [19] in 6061 aluminium alloy and by Hassan et al. [24] in 7010 aluminium alloy. In friction-stir-welded 2024 aluminium alloy, AGG has been reported by Safarkhanian et al. [9], Cerri et al. [11], Hu et al. [12], Yuan et al. [14], and Pang et al. [15]. Ipekoglu et al. [17] and Kalinenko et al. [19] have observed the AGG in 6061 aluminium alloy. In 6082 aluminium alloy, this undesirable process was found by Cerri et al. [18]. In this study, the relatively low microstructural stability against AGG was attributed to the inhomogeneous microstructure distribution within the stir zone produced during FSW. In 7075 aluminium alloy, AGG has been reported by Charit et al. [25], Ipekoglu et al. [26], Goloborodko et al. [28], and Sajadifar et al. [31]. Sharma et al. [27] observed this phenomenon in 7039 aluminium alloy, while Lezaack et al. [32] detected it in the 7474-T7351 alloy.

The abnormal grain growth in these alloys has been explained by the Humphreys cellular theory [38,39], which considers the simultaneous effects of grain refinement and precipitate dissolution that occur during FSW [24,25,39–45]. However, many aspects of this phenomenon remain unclear.

Recent works [46,47] have reported that abnormal microstructural coarsening can occur in FSWed heat-treatable aluminium alloys in the very early stages of post-weld heat treatments. More specifically, the abnormal grain growth may indeed develop during the heating stage of the solution treatment, which is the time period over which the FSW is heated from room temperature to the target solution annealing temperature. Considering that precipitations occur in heat-treatable aluminium alloys well below the solution annealing temperature, they may also occur at a very early stage of the post-weld solution treatment, particularly during the heating step. The evolution of precipitation can affect the abnormal microstructural coarsening, and the quantitative characterisation of this transient effect is not straight forward. Conventionally, the precipitates' characteristics (i.e., size and distribution) in the *as-welded state* have been used to predict grain-structure evolutions during the subsequent post-weld annealing heat treatments. However, their intermediate statuses and effects have not been considered [24,25,40–43,45]. This is because the precipitation size and volume fraction may vary substantially during the heating stage before reaching the solution annealing temperature.

Despite the existence of a considerable volume of work on precipitation behaviours in this class of materials by various research groups, to the best of the authors' knowledge, there is clearly a lack of available research on the evolution of precipitation and grain growth in the very early stage of heat treatment (i.e., the heating stage).

Hence, the aim of the present study was to clarify the microstructural changes that occur during the heating stage of post-weld solution heat treatments. The goal was to shed light on the nature of AGG, which often occurs in heat-treatable aluminium alloys during post-FSW heat treatments, and thus understand the associated underlying mechanisms. Moreover, the obtained results can be used for the optimization of key process parameters of industrial heat treatments of aluminium alloy welds made using FSW.

2. Materials and Methods

An AA2519 aluminium alloy with a chemical composition of Al–5.64 Cu–0.33 Mn–0.23 Mg–0.15 Zr–0.11 Ti–0.09 V–0.08 Fe–0.08 Zn–0.04 Sn–0.01 Si (in weight %) was produced using a semi-continuous casting method at the Research Equipment Sharing Center "Technology and Materials" at Belgorod State National Research University. This was a heat-treatable aluminium alloy with a relatively well studied FSW performance and ageing behaviour. The as-cast cylindrical ingot, with dimensions of 200 mm × 125 mm (height × diameter), was homogenised (i.e., 10 h at 380 °C, followed by 14 h at 510 °C), swaged with a total strain (ε) of ~2, and rolled to an ε of 1.4 (i.e., 75% reduction) at ~425 °C. To obtain a T820 peak ageing condition, rolled plates with dimensions of 150 mm × 50 mm × 3.75 mm (length × width × thickness) were solution-annealed at 525 °C for 1 h, followed by further cold rolling to a final thickness of 3 mm (i.e., a 20% reduction (ε of ~0.22)). The 3 mm plates were then artificially aged at 165 °C for 6 h. This condition is hereafter referred to as the *base material* (BM).

The aged plates were butt-welded using a commercial AccuStir 1004 FSW machine (General Tool Company, Cincinnati, OH, USA). The welding tool was fabricated from tool steel and consisted of a concave-shaped shoulder with a 12.5 mm diameter and an M5 cylindrical probe (pin) with a 2.7 mm length. To explore the effect of heat input during FSW on the microstructural evolution, two welding trials were conducted with different process parameters (Table 1). These included (i) a combination of a lower spindle rotational speed and a faster travers speed (i.e., feed rate), which resulted in a lower temperature during FSW, followed by a higher post-weld cooling rate, and (ii) a combination of a higher spindle rotational speed and a slower travers speed, which resulted in a higher temperature during FSW and a slower post-weld cooling rate [48]. The former is referred to as the low-heat-input weld and the latter is referred to as the high-heat-input weld throughout this work. These two regimes were selected based on the results of previous experiments [46]. For both cases, FSW was performed under plunge-depth control at a tool tilting angle of 2.5° on a stainless-steel backing plate.

**Table 1.** FSW conditions applied in this work.

Weld Designation	Spindle Rate (rpm)	Feed Rate (mm/min)
Low-heat-input (LHI) weld	500	760
High-heat-input (HHI) weld	1100	380

To simulate the heating stage of the post-weld solution heat treatment (SHT), the following procedure was implemented: The welded samples, each with a 3.0 mm diameter round K-type thermocouple embedded at a depth of 1.5 mm and located at the centre of the weld, were placed in a furnace that was preheated to 525 °C. The temperature profiles were continuously registered and monitored (Figure 1) using a Fluke (model 54IIB) data logger. For each case, once the temperature reached the target temperature, the sample was immediately quenched in cold water. The target solution annealing temperatures that were investigated were 300 °C, 400 °C, 450 °C, 485 °C, 500 °C, and 525 °C.

The microstructural evolution associated with the heating stage of the post-weld heat treatments was examined using optical microscopy (OM), backscatter electron scanning electron microscopy (BSE-SEM), and transmission electron microscopy (TEM). Standard sample preparation procedures were used, the details of which are described elsewhere [49–52].

Microstructural observations were made using an FEI Quanta 600 FEG-SEM (FEI Company, Hillsboro, OR, USA) operated with an accelerating voltage of 30 kV and a 100 μm diameter aperture. In addition to general microstructural observations, special emphasis was placed on the analysis of second-phase particles. For this purpose, the acquired backscattered SEM micrographs were processed using in-house-developed software in MATLAB [53]. The micrographs were initially filtered to reduce noise while preserving the intensity gradients between microstructural features using Gaussian filtering. They were then subjected to watershed segmentation to differentiate the precipitates from the

background. Due to the penetration of the electron beam into the material during image acquisition using SEM, the micrographs contained the precipitates lying below the sample surface. The watershed segmentation transformation was carefully executed to eliminate the sub-surface precipitates and only include those on the surface. Following the detection and recognition of the precipitates of interest, their sizes were measured using the equivalent circle diameter method.
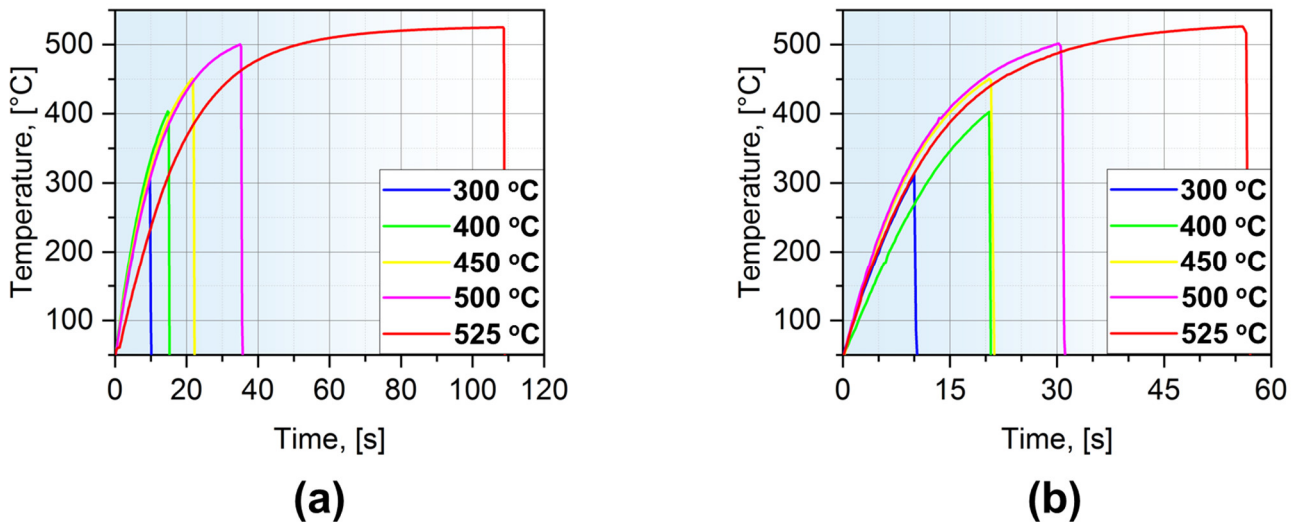
Figure 1. Temperature–time profiles recorded during the heating stages of the solution heat treatments at different target temperatures of the (**a**) low-heat-input weld and (**b**) high-heat-input weld.

For the observations using TEM, thin foils were obtained using electro-polishing in a solution of 25% nitric acid in ethanol with an applied potential of 20 V using a Struers Tenupol-5 twin-jet electro-polishing machine (Struers, Copenhagen, Denmark). The thin foils were examined using a JEM-2100EX TEM (JEOL Ltd., Tokyo, Japan) system equipped with a double-tilt stage and operating with an accelerating voltage of 200 kV. The TEM was also equipped with an energy-dispersive X-ray analyser (EDAX) manufactured by Oxford Instruments, which was used for the acquisition of EDX spectra at the locations of interest.

3. Results

### 3.1. The Temperature–Time Curves of the Heating Experiment

Figure 1 shows the temperature–time profiles recorded during the heating stage of the SHT conducted on the samples welded at different temperatures. The temperature increased rapidly at the beginning of the process and slowed down near the target temperature. Generally, the heating stage took between 1 and 2 min; it was therefore relatively short. Note that the negligible scatter in the heating rate for the various trials was likely associated with the manual handling of the samples into and out of the furnace.

3.2. Observations Using Optical Microscopy

The changes in the microstructure that occurred during the heating stage were initially assessed using low-magnification optical microscopy (Figures 2 and 3). For both welding conditions, the FSW-induced fine-grain structure was found to be stable up to 450 °C (Figures 2a and 3a). However, further increases in the temperature resulted in substantial microstructural changes with distinctly different characteristics for the examined welds.
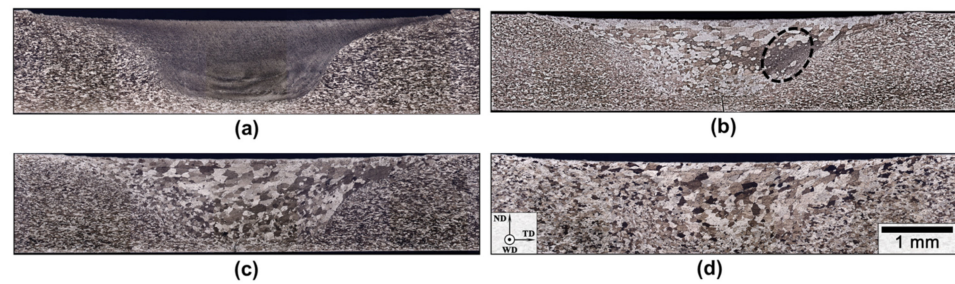
Figure 2. Effect of heating to various target temperatures on the microstructure evolution in the low-heat-input weld: (**a**) 450 °C, (**b**) 485 °C, (**c**) 500 °C, and (**d**) 525 °C. The magnification is the same in all micrographs. The reference frame for all cases is shown in (**d**). The normal direction, welding direction, and transverse direction are denoted as ND, WD, and TD, respectively. In all micrographs, the retreating side is on the left and the advancing side is on the right. See Section 3.2.1 for details.
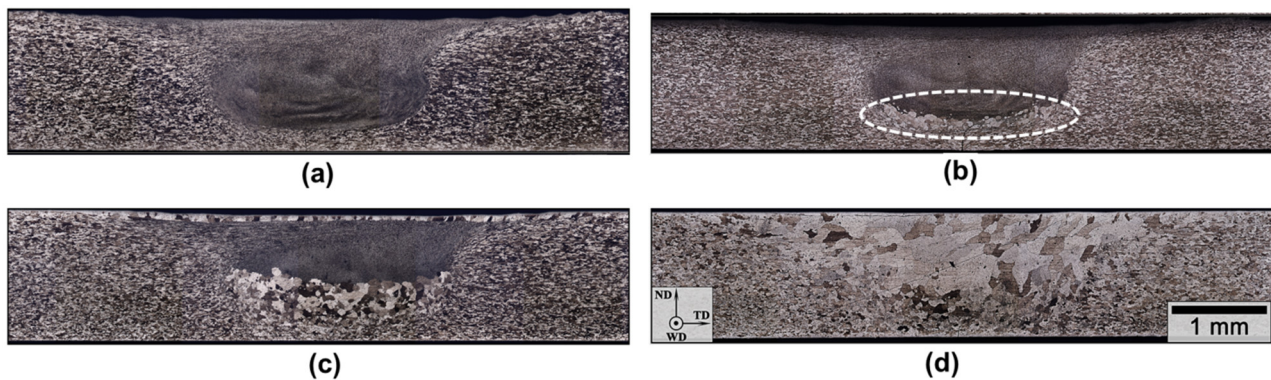
Figure 3. Effect of heating to various target temperatures on the microstructure evolution in the high-heat-input weld: (**a**) 450 °C, (**b**) 485 °C, (**c**) 500 °C, and (**d**) 525 °C. The magnification is the same in all micrographs. The reference frame for all welds is shown in (**d**). The normal direction, welding direction, and transverse direction are denoted as ND, WD, and TD, respectively. The retreating side is on the left, and the advancing side is on the right. See Section 3.2.2 for details.

3.2.1. Low-Heat-Input Weld

In the weld produced in the low-heat-input condition, abrupt grain growth was observed in almost the entire stir zone upon heating to 485 °C (Figure 2b). The FSW-induced fine-grain structure appeared to persist only in a small region on the advancing side (i.e., the right) of the stir zone, which is encircled in Figure 2b. This was under a condition where a few grains in this region experienced drastic coarsening, resulting in a classic AGG appearance. From this observation, it can be deduced that the annealing behaviour upon heating was controlled by AGG.

Upon increasing the temperature to 500 °C, the abnormal grains continued to consume the remaining microstructure of the stir zone (Figure 2c). An additional increase in the temperature to 525 °C did not appear to cause further effects (Figure 2d). A previous report showed that an additional subsequent soaking of the sample at 525 °C for 1 h made no further changes to the grain structure [46]. Therefore, these observations suggest that the AGG was completed during the heating stage of SHT, before reaching the target temperature.

3.2.2. High-Heat-Input Weld

For the weld produced in the high-heat-input condition, no particular changes were observed during heating to 450 °C (Figure 3a), while heating to 485 °C resulted in local grain coarsening near the root of the stir zone (encircled in Figure 3b). Hence, the microstructure produced via this welding condition appeared to have higher thermal stability compared to that produced with a lower heat input.

By increasing the target temperature to 500 °C, the volume fraction of the grains consumed by AGG at the weld root significantly increased (Figure 3c). In addition, substantial microstructural coarsening was also observed in the shoulder-affected zone (SAZ), i.e., near the top surface of the stir zone shown in Figure 3c. Nevertheless, despite the substantial grain growth at the weld root and the SAZ, the microstructure at the centre of the stir zone appeared to remain almost unchanged, which was indicative of relatively high thermal stability (Figure 3c). Previous studies have also observed abnormal grain growth in the periphery of the stir zone [8,9,15,18,24–26,28,30,31,40–42,54–58].

Similar to the low-heat-input condition, upon reaching the solution annealing temperature, the large grains gradually consumed the microstructure in the stir zone (Figure 3d). Therefore, the AGG was also observed to be completed during the heating stage of the post-weld SHT in the high-heat-input weld, although the microstructure of this weld was seen to have higher thermal stability compared to that of the low-heat-input weld.

### 3.3. Observations Using SEM

The evolution of precipitates during the heating stage was investigated using SEM, and the necessary number of BSE micrographs were captured. In all cases, the examinations were focused on the centre of the stir zone. Examples of the acquired micrographs are shown in Figures 4–6, and the quantitative information extracted from the micrographs is presented in Table 2.
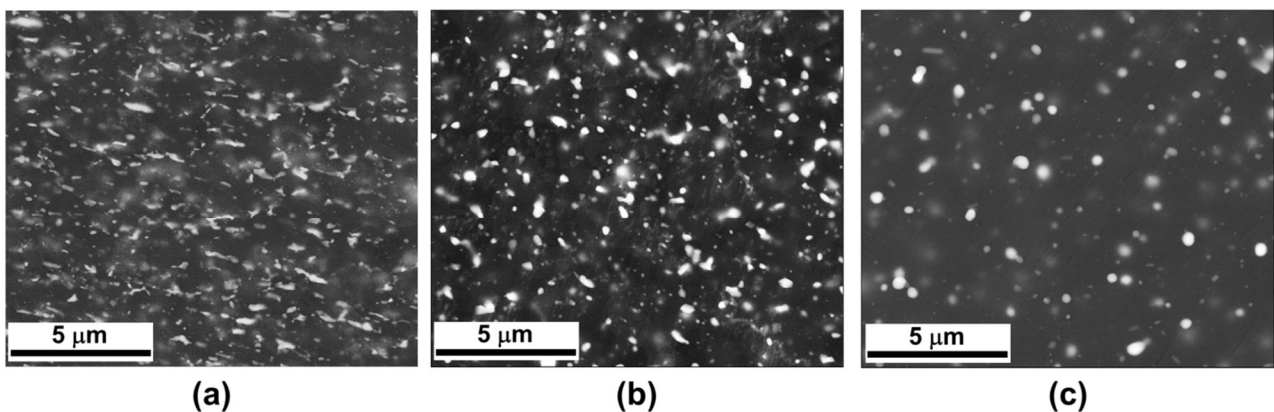

Figure 4. Typical backscatter electron images of the precipitates acquired from the central section of the stir zone of the low-heat-input weld (**a**) in the as-welded condition, (**b**) after heating to 450 °C, and (**c**) after heating to 500 °C.

Table 2. Effect of heating to different target temperatures on the precipitates' volume fraction and size.

Material Condition	Low-Heat-Input Weld		High-Heat-Input Weld	
	Mean Diameter (µm)	Volume Fraction (%)	Mean Diameter (µm)	Volume Fraction (%)
As-FSWed	0.11 ± 0.05	6.7	0.06 ± 0.05	3.0
Heated to 450 °C	0.12 ± 0.06	5.3	0.09 ± 0.05	6.0
Heated to 485 °C	0.14 ± 0.07	3.4	0.16 ± 0.09	7.8
Heated to 500 °C	0.18 ± 0.07	2.6	0.24 ± 0.07	4.6
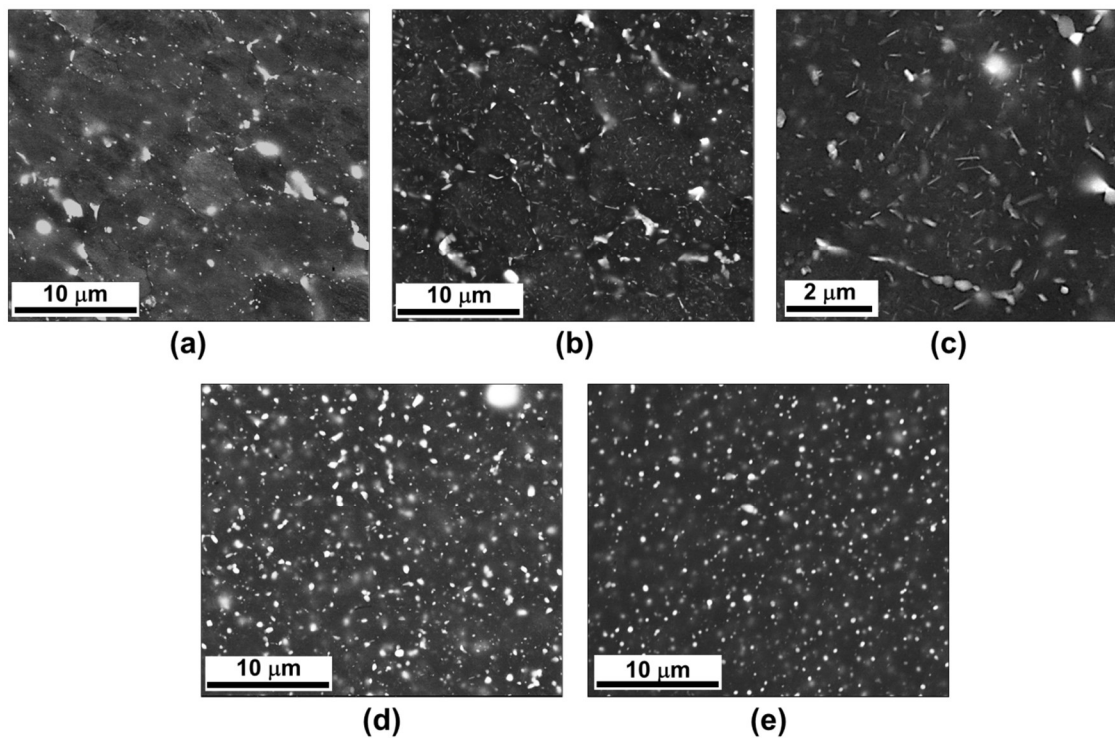
Figure 5. Typical backscatter electron images of the precipitates taken from the central section of the stir zone of the high-heat-input weld in (**a**) the as-welded condition, (**b**,**c**) after heating to 450 °C, (**d**) after heating to 485 °C, and (**e**) after heating to 500 °C.
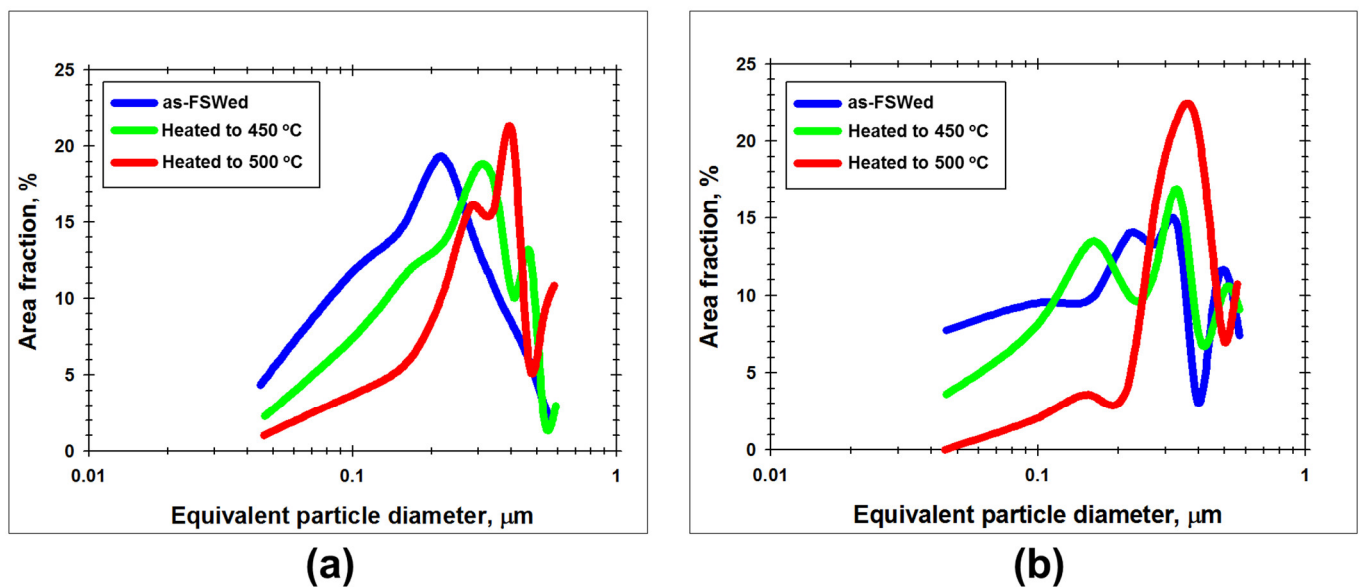
Figure 6. Plots of precipitate size distributions in the (**a**) low-heat-input weld and (**b**) high-heat-input weld after heating to 450 °C and 500 °C compared to the as-welded conditions.

3.3.1. Low-Heat-Input Weld

Figure 4a shows that the low-heat-input weld in the as-welded condition contained a significant fraction (≈7%) of relatively coarse precipitates (Table 2). This was in agreement with a previous observation made by Kalinenko et al. [59], where FSW in low-heat-input conditions led to precipitation coarsening, as opposed to precipitation dissolution, in the stir zone.

The results showed that the heating of the weld produced in a low-heat-input condition to 500 °C and above led to precipitate growth, as shown in Figures 4b,c and 6a and Table 2. Moreover, the volume fraction of the secondary precipitates decreased during heating with an increase in the target temperature (Table 2), implying that the precipitates were dissolved.

3.3.2. High-Heat-Input Weld

Analyses of the microstructures of the high-heat-input weld showed complex precipitation behaviours during heating to different solution temperatures. As shown in Figure 5a and Table 2, the microstructure of the stir zone in the as-welded condition contained a lower fraction of fine precipitates. This was likely due to the dissolution of the precipitates, which occurred during the FSW process. As can be seen in Figure 5a, the precipitates were often accommodated along the grain boundaries. This implies that they might have re-precipitated *following* FSW upon cooling to the ambient temperature.

During the heating of the high-heat-input weld to 450 °C, the intergranular precipitates became substantially coarsened (Figure 5b) and their volume fraction increased (Table 2). The latter implies that the precipitates were nucleated from a supersaturated solid solution during heating. The preferential nucleation of the precipitates at grain boundaries can be linked with the fine-grained structure of the stir zone. Moreover, the nucleation of nanoscale needle-shaped precipitates was also observed in the grain interior (Figure 5c). Considering the needle-shaped morphology of these precipitates (Figure 5c), it is likely that they had preferential growth in directions that had coherency (or semi-coherency) with the matrix.

The complex precipitation behaviours observed in the weld produced with a high-heat input led to bimodal distributions of their area fraction, as shown in Figure 6b and Table 2.

Heating to a higher target temperature (i.e., 485 °C) further promoted precipitation coarsening (Table 2 and Figure 6b) and spheroidisation (Figure 5d), the latter of which could have been due to the loss of coherency with the matrix. After reaching the target temperature of 500 °C, the precipitates' volume fraction was reduced (Table 2 and Figure 5e), which was indicative of their dissolution.

3.4. Observations Using TEM

TEM observations of the weld microstructures were acquired to obtain additional insight into the precipitation phenomenon. Typical micrographs taken from the stir zones of the low- and high-heat-input welds following heating to different temperatures are presented in Figures 7 and 8, respectively.
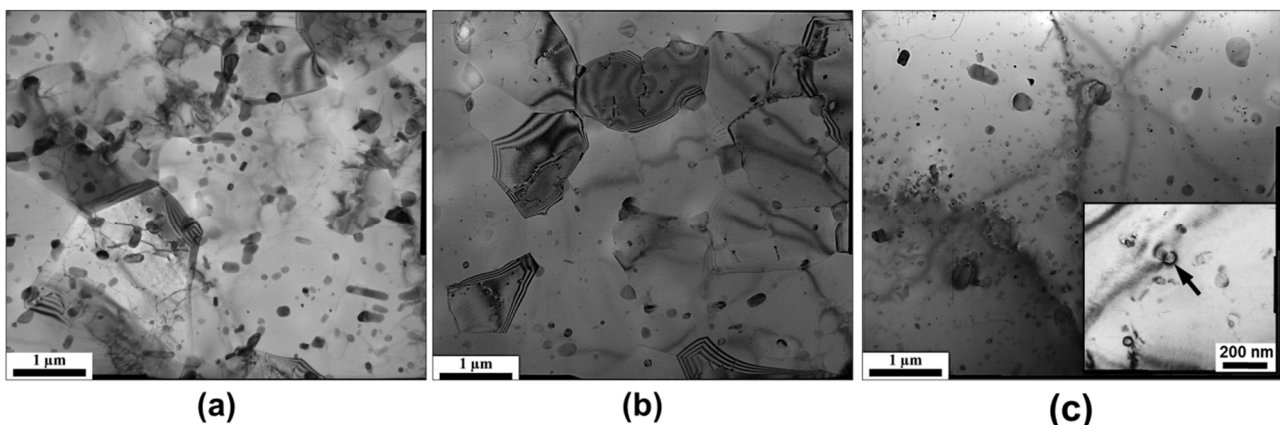
Figure 7. Representative bright-field TEM micrographs of the microstructure in the stir zone of the low-heat-input weld (**a**) in the as-welded condition and after subsequent heating to (**b**) 450 °C and (**c**) 500 °C. In (**c**), the insert in the bottom right corner shows a higher-magnification image of the microstructure. See Section 3.4 for details.
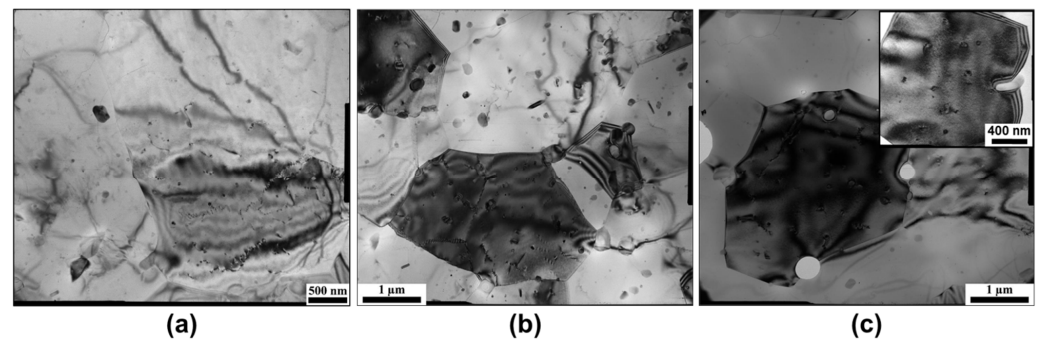
Figure 8. Representative bright field TEM micrographs of the microstructure in the stir zone of the high-heat-input weld (**a**) in the as-welded condition and after subsequent heating to (**b**) 450 °C and (**c**) 500 °C. In (**c**), the insert in the top right corner shows a higher-magnification image of the microstructure.

In agreement with the observations made using SEM, a relatively high volume fraction of secondary precipitates was observed in the as-welded condition of the low-heat-input weld (Figure 7a). Meanwhile, upon heating to 450 °C during the post-weld heat treatment, the precipitates increased in size and concurrently dissolved (Figure 7b). In contrast, the high-heat-input weld contained a low fraction of precipitates in the as-welded condition (Figure 8a). However, the post-weld heating to different temperatures appeared to have resulted in the nucleation (Figure 8b) and coarsening of precipitates (Figure 8c).

The observations made using TEM suggest that in the microstructures of both welds, heating above 450 °C led to nanoscale precipitates, as shown in the high-magnification inserts in Figures 7c and 8c. In some cases, these precipitates had the characteristic coffee-bean contrast (as highlighted by the arrow in the high-magnification insert in Figure 7c) and were therefore coherent with the matrix.

To acquire additional information on the secondary precipitates, a TEM-EDS analysis was carried out, and the results are summarised in Figure 9. The results suggest that θ-phase (Al_2Cu) was the dominant precipitate in the microstructure of the stir zone (Figure 9a), although a measurable portion of T-phase ($Al_{20}Cu_2Mn_3$) was also revealed (Figure 9b). The nanoscale precipitates that appeared in the heat-treated weld at the near-solution annealing temperatures were identified as β′ (Al_3Zr)-phase (Figure 9c). It is worth noting that the density of the revealed non-homogeneously distributed β′-phase was relatively low. It was therefore unlikely that these particles had a substantial influence on the grain growth behaviour.
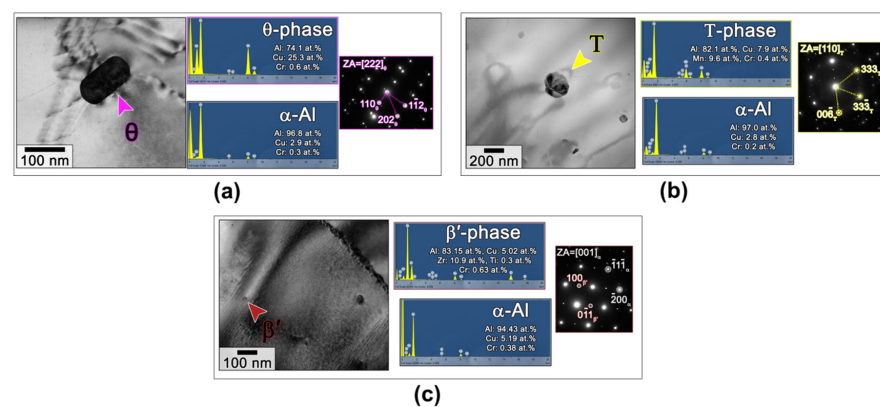
Figure 9. Bright-field TEM micrographs, EDS spectra, and selected area electron diffraction patterns of typical precipitates: (**a**) θ-phase in the low-heat-input weld heated to 450 °C, (**b**) T-phase in the low-heat-input weld heated to 480 °C, and (**c**) β′-phase in the high-heat-input weld heated to 450 °C. The Cr peaks in the EDS spectra are artefacts associated with the TEM specimen holder. Note that the aluminium matrix was supersaturated with copper. See Section 3.4 for details.

4. Discussion

4.1. Impact of Heat Input on Precipitation and Grain Growth

The results of these investigations demonstrated that, firstly, the AGG in the FSWed heat-treatable Al–Cu–Mg alloy was indeed completed during the heating stage of the post-weld solution treatment. Secondly, this was preceded and then accompanied by a complex precipitation evolution, including the dissolution/growth of the existing precipitates and the nucleation and growth of new precipitates. Interestingly, the latter was significantly affected by the heat input during the FSW process.

In the *low-heat-input* condition, the precipitates simultaneously underwent coarsening and dissolution (Figures 4, 6a and 7 and Table 2), which could be linked to the relatively low temperature obtained during FSW (i.e., not sufficiently high to dissolve them). As a result, there was no supersaturated solid solution in the stir zone for additional precipitation to occur during subsequent heating. Both coarsening and dissolution phenomena reduce the Zener pinning force and thereby deteriorate the thermal stability of a weld's microstructure, which in this case resulted in rapid abnormal grain growth during the heating stage of the post-weld solution treatment (Figure 2).

In the *high-heat-input* welding condition, the temperature during the FSW likely reached temperatures high enough to dissolve the precipitates (i.e., leading to a solid solution). Upon cooling following the FSW and during the heating stages of the subsequent heat treatments, partial re-precipitation occurred from the supersaturated solid solution (Figures 5 and 8 and Table 2). Owing to the relatively fine-grained structure of the stir zone, precipitates were observed to nucleate at grain boundaries (Figure 5b). The results of a previous study on an FSWed microalloyed steel showed that the precipitates tended to nucleate at dislocation entanglement sites as well as at grain boundaries (both high and low angles) [60]. This was associated with the high level of shear strain induced during FSW at high temperatures (i.e., strain-induced precipitation). This could have been the case for the material in this study. On the other hand, the precipitates nucleated in the grain interior were relatively fine in size and were likely to be coherent with the matrix (Figure 5c). All these details contributed to a relatively high pinning pressure, and as a result, a higher thermal stability was observed for this weld. At temperatures close to the solution annealing temperature, however, the precipitates tended to spheroidise, coarsen, and show evidence of incoherency with the matrix grains (Figure 5d,e). This eventually resulted in grain growth (Figure 3d).

4.2. Relevance to Humphreys' Cellular Model

The thermal stability of welded materials has often been described using Humphreys' cellular theory [38,39]. Based on this model, the annealing behaviour of a particle-containing material is dependent on the volume fraction of the particles (F_v), the average grain radius (R), and the mean particle size (d). This has been defined as a dimensionless parameter via $Z = 3F_v R/d$. Depending on the magnitude of the Z parameter, different annealing behaviours are expected, as classified in Table 3. Importantly, this model is only valid for a microstructure with uniformly distributed particles that are not coherent with the matrix.

Table 3. Potential microstructural response to solution annealing based on the Humphreys cellular model.

Parameter Z	Predicted Annealing Behaviour
$0 < Z < 0.1$	Normal grain growth
$0.1 < Z < 0.25$	Normal grain growth and abnormal grain growth
$0.25 < Z < 1.0$	Abnormal grain growth
$Z > 1.0$	No grain growth. Microstructure stability

The results of the present study suggest that AGG occurred in the investigated FSWed heat-treatable alloy concurrently with precipitation evolution. As a result, the precipitate's size, volume fraction, morphology, and even spatial distribution may have significantly

changed in comparison to the as-welded condition. A comparison between the material's responses to annealing and those predicted by Humphreys' cellular model is summarised in Table 4.

Table 4. Analysis of the weld annealing behaviour using the Humphreys cellular model.

Heating Temperature	Secondary Precipitates		Average Grain Radius (μm)	Z	Annealing Behaviour	
	Volume Fraction (%)	Mean Size (μm)			Predicted	Observed
Low-heat-input weld						
20 °C	0.067	0.11		1.65	No grain growth	No grain growth
450 °C	0.053	0.12	0.90	1.20		
485 °C	0.034	0.14		0.65	Abnormal grain growth	Abnormal grain growth
High-heat-input weld						
485 °C	0.078	0.16	1.75	2.55	No grain growth	No grain growth
500 °C	0.046	0.24	3.85	2.20	No grain growth	Normal grain growth

Note: The discrepancy between the predicted and observed behaviours is highlighted in grey.

In the *low-heat-input* condition, excellent agreement was obtained between the experimentally observed and predicted results (Table 4). This implies that the low thermal stability of the welded material in this case (Figure 2) can be explained on the basis of relatively fine grains with comparatively coarse secondary particles, which were both produced during the low-heat-input FSW.

In the *high-heat-input* condition, however, the experimentally observed data did not show good convergence towards the predictions made by the Humphreys model (Table 4). Due to the heterogeneous precipitation of dispersoids at grain boundaries (Figure 5b) as well as their coherent nucleation within hosting grains during the heating stage (Figure 5c), the model has only limited applicability. It can only be used for microstructures that evolve at relatively high heating temperatures, in which the particles are almost uniformly distributed throughout the material and have already lost their coherency with the matrix (Figure 5d,e). Even in such cases, the model may result in erroneous predictions, as highlighted in Table 4.

4.3. Outlook

The present work provides a useful insight into the abnormal grain growth behaviour during the post-weld heating of a friction-stir-welded AA2519-T820 aluminium alloy. Nevertheless, there are still several areas that deserve additional attention in future works, some of which are highlighted in the following sections.

4.3.1. Final Size of Abnormal Grains

By comparing Figure 2d with Figure 3d, it was evident that the final size of the abnormal grains in the low-heat weld was smaller than that in the low-heat-input weld. This observation agreed with a number of previous works in the scientific literature [19,46]. Hence, lowering the FSW heat input may be an effective approach for suppressing AGG during a post-weld solution treatment. However, the origin of this important effect is still unclear.

4.3.2. Microstructural Behaviour at the Periphery of the Stir Zone

The AGG in FSWed materials often begins in the periphery of the stir zone [8,9,15,18,24–26,28,30,31,40–42,54–58]. Specifically, in high-heat-input conditions, the preferential microstructural coarsening occurred in the near-surface layer or at the weld root (Figure 3c). On the other hand, the thermal stability of the advancing side of the

low-heat-input weld (Figure 2b) was relatively high. The origin of these phenomena is still not understood and requires further study.

4.3.3. Theory of Orientation Growth

From the present study, it seems that AGG is closely linked with precipitation phenomena and can typically be explained in terms of Humphreys' cellular model. On the other hand, there are several works in the scientific literature reporting the formation of a specific crystallographic texture during AGG [19,61]. By analogy with the recrystallization texture, this interesting phenomenon could be explained by either the preferential growth of grains of a particular crystallographic orientation (i.e., the so-called orientation nucleation theory) or the preferential migration of grain boundaries of a particular misorientation (i.e., the so-called orientation growth theory) [62]. Kalinenko et al. [19] revealed no clear correlation between the grains with low stored energy in the as-FSWed condition and the final AGG texture. Hence, it was concluded that texture formation is unlikely to be explained in terms of the orientation nucleation theory, and therefore this phenomenon was presumed to be associated with the preferential migration of $40^{\circ}<111>$ grain boundaries [61]. If so, the catastrophic grain growth in FSWed materials may be governed by at least two mechanisms: (i) precipitation pinning and (ii) orientation growth. This concept provides an additional explanation for the revealed deviations from Humphreys' cellular theory, as discussed in Section 4.2. However, the possible interrelation between these two microstructural mechanisms and their mutual contribution to the global grain growth process are not clear and thus deserve further study.

5. Conclusions

The early stages of abnormal grain growth were investigated in friction-stir-welded AA2519 processed in T820 temper. A series of experiments were conducted to simulate the heating stage of the post-weld solution treatment. The produced microstructures were examined using optical metallography, BSE-SEM, and TEM techniques. To explore the potential influence of FSW conditions, welds were produced in lower- and higher-heat-input conditions by applying different process parameters. The major results derived from this study are as follows:

(1) The welded materials experienced drastic microstructural changes after the relatively short duration of the heating stage ($\approx$1–2 min). These included abnormal grain growth and a complex sequence of precipitation and dissolution phenomena. All microstructural processes were strongly influenced by the thermal condition of the preceding FSW.

(2) In the *low-heat-input* condition, the temperature attained during the FSW was insufficient for the dissolution of the second-phase precipitates. Therefore, the subsequent heating resulted in the coarsening of the retained particles and their subsequent dissolution. Both of these processes reduced the Zener force and thus deteriorated the microstructure's thermal stability. Accordingly, the microstructural coarsening in these welds progressed very rapidly.

(3) In the *high-heat-input* condition, the precipitates mainly dissolved during the FSW, thus producing a supersaturated solid solution. Consequently, the post-weld heating resulted in the re-precipitation of fine precipitates in the grain interior. Moreover, due to the microstructure (fine-grained) of the stir zone, the particles re-precipitated at grain boundaries. All these effects resulted in effective grain pinning and thus provided higher thermal stability. With an increase in the heating temperature, however, the particles coarsened and then dissolved, thereby triggering abnormal grain growth.

(4) Considering the heterogeneous precipitation of secondary precipitates at grain boundaries, Humphreys' cellular theory had limited applicability for the analysis of the welds produced in high-heat-input conditions.

References

1. Thomas, W.M.; Nicholas, E.D.; Needham, J.C.; Murch, M.G.; Templesmith, P.; Dawes, C.J. Friction stir welding. G.B. Patent Application N0. 9125978, 8 December 1991.
2. Aldanondo, E.; Vivas, J.; Álvarez, P.; Hurtado, I.; Karanika, A. Friction Stir Welding of AA2099-T83 and AA2060-T8E30 Aluminium Alloys with New Cr-Free Surface Treatments and Sealant Application. *Metals* **2021**, *11*, 644. [CrossRef]
3. Aldanondo, E.; Zubiri, O.; Vivas, J.; Álvarez, P.; Hurtado, I. Fretting Fatigue as a Limiting Factor on the Durability of Friction Stir Welded Lap Joints Using AA2099-T83 and AA2060-T8E30 Aluminium Alloys. *J. Manuf. Mater. Process.* **2022**, *6*, 94. [CrossRef]
4. Aldanondo, E.; Vivas, J.; Álvarez, P.; Hurtado, I. Effect of Tool Geometry and Welding Parameters on Friction Stir Welded Lap Joint Formation with AA2099-T83 and AA2060-T8E30 Aluminium Alloys. *Metals* **2020**, *10*, 872. [CrossRef]
5. Mishra, R.S.; Ma, Z.Y. Friction stir welding and processing. *Mater. Sci. Eng. R* **2005**, *50*, 1–78. [CrossRef]
6. Threadgill, P.L.; Leonard, A.J.; Shercliff, H.R.; Withers, P.J. Friction stir welding of aluminum alloys. *Int. Mater. Rev.* **2009**, *54*, 49–93. [CrossRef]
7. Liu, F.C.; Xiao, B.L.; Wang, K.; Ma, Z.Y. Investigation of superplasticity in friction stir processed 2219Al alloy. *Mater. Sci. Eng.* **2010**, *527*, 4191–4196. [CrossRef]
8. Attallah, M.M.; Salem, H.G. Friction stir welding parameters: A tool for controlling abnormal grain growth during subsequent heat treatment. *Mater. Sci. Eng.* **2005**, *391*, 51–59. [CrossRef]
9. Safarkhanian, M.A.; Goodarzi, M.; Boutorabi, S.M.A. Effect of abnormal grain growth on tensile strength of Al-Cu-Mg alloy friction stir welded joints. *J. Mater. Sci.* **2009**, *44*, 5452–5458. [CrossRef]
10. Liu, H.J.; Feng, X.L. Effect of post-processing heat treatment on microstructure and microhardness of water-submerged friction stir processed 2219-T6 aluminum alloy. *Mater. Design* **2013**, *47*, 101–105. [CrossRef]
11. Cerri, E.; Leo, P. Mechanical properties evolution during post-weld-heat treatments of double-lap friction stir welded joints. *Mater. Design* **2011**, *32*, 3465–3475. [CrossRef]
12. Hu, Z.L.; Wang, X.S.; Pang, Q.; Huang, F.; Qin, X.P.; Hua, L. The effect of postprocessing on tensile property and microstructure evolution of friction stir welding aluminum alloy joint. *Mater. Character.* **2015**, *99*, 180–187. [CrossRef]
13. Huang, Y.X.; Wan, L.; Lv, Z.L.; Lv, S.X.; Zhou, L.; Feng, J.C. Microstructure and microhardness of aluminium alloy friction stir welds with heat treatment. Formability and microstructural stability of friction stir welded Al alloy tube during subsequent spinning and post weld heat treatment. *Sci. Technol. Weld. Join* **2016**, *21*, 638–644. [CrossRef]
14. Yuan, S.J.; Hu, Z.L.; Wang, X.S. Formability and microstructural stability of friction stir welded Al alloy tube during subsequent spinning and post weld heat treatment. *Mater. Sci. Eng.* **2012**, *558*, 586–591. [CrossRef]
15. Pang, Q.; Zhang, J.H.; Huq, M.J.; Hu, Z.L. Characterization of microstructure, mechanical properties and formability for thermomechanical treatment of friction stir welded 2024-O alloys. *Mater. Sci. Eng.* **2019**, *765*, 138303. [CrossRef]
16. Yadav, V.K.; Gaur, V.; Singh, I.V. Effect of Post-Weld Heat Treatment on Mechanical Properties and Fatigue Crack Growth Rate in Welded AA-2024. *Mater. Sci. Eng.* **2020**, *779*, 139116. [CrossRef]
17. Ipekoglu, G.; Erim, S.; Cam, G. Investigation into the influence of post-weld heat treatment on the friction stir welded AA6061Al-alloy plates with different temper conditions. *Metal. Mater. Trans.* **2014**, *45*, 864–877. [CrossRef]
18. Cerri, E.; Leo, P. Influence of high temperature thermal treatment on grain stability and mechanical properties of medium strength aluminium alloy friction stir welds. *J. Mater. Proc. Technol.* **2013**, *213*, 75–83. [CrossRef]
19. Kalinenko, A.; Vysotskii, I.; Malopheyev, S.; Mironov, S.; Kaibyshev, R. Relationship between welding conditions, abnormal grain growth and mechanical performance in friction-stir welded 6061-T6 aluminum alloy. *Mater. Sci. Eng.* **2021**, *817*, 141409. [CrossRef]

20. Zou, X.; Liu, C.; Deng, M.; Chen, J.; Zhang, L.; Chen, K. Inhibition of Abnormal Grain Growth in Stir Zone via In-Situ Intermetallic Particle Formation During Friction Stir Welding of AA6061. *Acta Metall. Sin.* **2023**, *36*, 597–610. [CrossRef]

21. Singh, R.K.; Guraja, S.S.S.; Ajide, O.O.; Owolabi, G.M.; Kumar, N. Investigation of Initial Metallurgical Factors on the Dynamic Impact Response and Adiabatic Shear Bands Formation of the 6061 Al Alloy. *Mater. Sci. Eng.* **2023**, *865*, 144636. [CrossRef]

22. Baghdadi, A.H.; Sajuri, Z.; Omar, M.Z.; Rajabi, A. Friction Stir Welding Parameters: Impact of Abnormal Grain Growth during Post-Weld Heat Treatment on Mechanical Properties of Al–Mg–Si Welded Joints. *Metals* **2020**, *10*, 1607. [CrossRef]

23. Vysotskiy, I.V.; Malopheyev, S.S.; Mironov, S.Y.; Kaibyshev, R.O. Optimization of Friction-Stir Welding of 6061-T6 Aluminum Alloy. *Phys. Mesomech.* **2020**, *23*, 402–429. [CrossRef]

24. Hassan, K.A.A.; Norman, A.F.; Price, D.A.; Prangnell, P.B. Stability of nugget zone grain structure in high strength Al-alloy friction stir welds during solution treatment. *Acta Mater.* **2003**, *57*, 1923–1936. [CrossRef]

25. Charit, I.; Mishra, R.S. Abnormal grain growth in friction stir processed alloys. *Scr. Mater.* **2008**, *58*, 367–371. [CrossRef]

26. Ipekoglu, G.; Erim, S.; Cam, G. Effects of temper condition and post weld treatment on the microstructure and mechanical properties of friction stir butt-welded AA7075 Al alloy. *Int. Adv. Manuf. Technol.* **2014**, *70*, 201–213. [CrossRef]

27. Sharma, C.; Dwivedi, D.K.; Kumar, P. Effect of post weld heat treatments on microstructure and mechanical properties of friction stir welded joints of Al-Zn-Mg alloy AA7039. *Mater. Des.* **2013**, *43*, 134–143. [CrossRef]

28. Goloborodko, A.; Ito, T.; Yun, X.; Motohashi, Y.; Itoh, G. Friction stir welding of a commercial 7075-T6 aluminum alloy: Grain refinement, thermal stability and tensile properties. *Mater. Trans.* **2004**, *45*, 2503–2508. [CrossRef]

29. Ren, S.; Ma, Z.; Chen, L.; Zhang, Y. Effects of post-weld heat-treatment and second-welding on tensile properties of friction stir welded 7075-T651 aluminum alloy. *Acta Metal. Sin.* **2007**, *43*, 225–230.

30. Han, P.; Yang, C.; Wang, J.; Du, B.; Liu, X.; Xue, P.; Ma, Z.; Ni, D. Effects of solution heat treatment on friction stir welding joints of 7B04-O aluminum alloy. *J. Mech. Eng.* **2015**, *51*, 35–41. [CrossRef]

31. Sajadifar, S.V.; Moeini, G.; Scharifi, E.; Lauhoff, C.; Bohm, S.; Niendorf, T. On the effect of quenching on postweld heat treatment of friction-stir-welded aluminum 7075 Alloy. *J. Mater. Eng. Perform.* **2019**, *28*, 5255–5265. [CrossRef]

32. Lezaack, M.B.; Simar, A. Avoiding abnormal grain growth in thick 7XXX aluminium alloy friction stir welds during T6 post heat treatments. *Mater. Sci. Eng.* **2021**, *807*, 140901. [CrossRef]

33. Jandaghi, M.R.; Badini, C.; Pavese, M. Dissimilar friction stir welding of AA2198 and AA7475: Effect of solution treatment and aging on the microstructure and mechanical strength. *J. Manuf. Proc.* **2020**, *57*, 712–724. [CrossRef]

34. Dong, J.; Zhang, D.; Zhang, W.; Cao, G.; Qiu, C. Effect of Post-Weld Heat Treatments on the Microstructure and Mechanical Properties of Underwater Friction Stir Welded Joints of 7003-T4/6060-T4 Aluminium Alloys. *Mater. Sci. Eng.* **2023**, *862*, 144423. [CrossRef]

35. Baghdadi, A.H.; Sajuri, Z.; Keshtgar, A.; Mohd Sharif, N.; Rajabi, A. Mechanical Property Improvement in Dissimilar Friction Stir Welded Al5083/Al6061 Joints: Effects of Post-Weld Heat Treatment and Abnormal Grain Growth. *Materials* **2022**, *15*, 288. [CrossRef] [PubMed]

36. Jandaghi, M.R.; Pouraliakbar, H.; Saboori, A.; Hong, S.I.; Pavese, M. Comparative Insight into the Interfacial Phase Evolutions during Solution Treatment of Dissimilar Friction Stir Welded AA2198-AA7475 and AA2198-AA6013 Aluminum Sheets. *Materials* **2021**, *14*, 1290. [CrossRef]

37. Zhang, C.; Huang, G.; Zhang, D.; Sun, Z.; Liu, Q. Microstructure and Mechanical Properties in Dissimilar Friction Stir Welded AA2024/7075 Joints at High Heat Input: Effect of Post-Weld Heat Treatment. *J. Mater. Res. Technol.* **2020**, *9*, 14771–14782. [CrossRef]

38. Humphreys, F.J. A unified theory of recovery, recrystallization and grain growth, based on the stability and growth of cellular microstructures—I. The basic model. *Acta Mater.* **1997**, *45*, 4231–4240. [CrossRef]

39. Humphreys, F.J. A unified theory of recovery, recrystallization and grain growth, based on the stability and growth of cellular microstructures—II. The effect of second-phase particles. *Acta Mater.* **1997**, *45*, 5031–5039. [CrossRef]

40. Chen, Y.; Ding, H.; Li, J.; Cai, Z.; Zhao, J.; Yang, W. Influence of multi-pass friction stir processing on the microstructure and mechanical properties of Al-5083 alloy. *Mater. Sci. Eng.* **2016**, *650*, 281–289. [CrossRef]

41. Mironov, S.; Masaki, K.; Sato, Y.S.; Kokawa, H. Relationship between material flow and abnormal grain growth in friction-stir welds. *Scr. Mater.* **2012**, *67*, 983–986. [CrossRef]

42. Chen, K.; Gan, W.; Okamoto, K.; Kwansoo, C.; Wagoner, R.H. The mechanism of grain coarsening in friction-stir-welded AA5083 after heat treatment. *Metal. Mater. Trans.* **2011**, *42*, 488–507. [CrossRef]

43. Kumar, N.; Mishra, R.S. Thermal stability of friction stir processed ultrafine grained AlMgSc alloy. *Mater. Character.* **2012**, *74*, 1–10. [CrossRef]

44. Guo, J.; Lee, B.Y.; Du, Z.; Bi, B.G.; Tan, M.J.; Wei, J. Effect of nano-particle addition on grain structure evolution of friction stir-processed Al 6061 during postweld annealing. *JOM* **2016**, *68*, 2268–2273. [CrossRef]

45. Jana, S.; Mishra, R.S.; Baumann, J.A.; Grant, G. Effect of process parameters on abnormal grain growth during friction stir processing of a cast Al alloy. *Mater. Sci. Eng.* **2010**, *528*, 189–199. [CrossRef]

46. Zuiko, I.S.; Mironov, S.; Betsofen, S.; Kaibyshev, R. Suppression of abnormal grain growth in friction-stir welded Al–Cu–Mg alloy by lowering of welding temperature. *Scr. Mater.* **2021**, *196*, 113765. [CrossRef]

47. Kalinenko, A.; Vysotskiy, I.; Malopheyev, S.; Mironov, S.; Kaibyshev, R. New insight into the phenomenon of the abnormal grain growth in friction-stir welded aluminum. *Mater. Letter.* **2021**, *302*, 130407. [CrossRef]

48. Baillie, P.; Campbell, S.W.; Galloway, A.M.; Cater, S.R.; McPherson, N.A. A comparison of double sided friction stir welding in air and underwater for 6mm S275 steel plate. *Int. J. Chem. Nucl. Metall. Mater. Eng.* **2014**, *8*, 651–655.
49. Zuiko, I.S.; Malopheyev, S.; Mironov, S.; Betsofen, S.; Kaibyshev, R. On the heterogeneous distribution of secondary precipitates in friction-stir-welded 2519 aluminum alloy. *Metals* **2022**, *12*, 671. [CrossRef]
50. Zuiko, I.S.; Kaibyshev, R. Ageing response of cold-rolled Al–Cu–Mg alloy. *Mater. Sci. Eng.* **2020**, *781*, 139148. [CrossRef]
51. Zuiko, I.; Kaibyshev, R. Effect of plastic deformation on the ageing behaviour of an Al–Cu–Mg alloy with a high Cu/Mg ratio. *Mater. Sci. Eng.* **2018**, *737*, 401–412. [CrossRef]
52. Zuiko, I.; Kaibyshev, R. Aging behavior of an Al–Cu–Mg alloy. *J. Alloys Compd.* **2018**, *759*, 108–119. [CrossRef]
53. The MathWorks Inc. *Image Processing ToolboxTM: (R2021b)*; The MathWorks Inc.: Natick, MA, USA, 2021; Available online: https://www.mathworks.com (accessed on 24 May 2023).
54. Yoshioka, H.; Fukumoto, S.; Yamamoto, A.; Tsubakino, H.; Okita, K.; Tomita, T. Effect of post weld heat treatment on mechanical properties and microstructures of friction stir welded AZ31B magnesium alloy. *J. Jap. Inst. Light Metal.* **2008**, *58*, 2–7. [CrossRef]
55. Dawson, H.; Serrano, M.; Cater, S.; Jimenez-Melero, E. Characterization of ODS steel friction stir welds and their abnormal grain growth behavior. *Fusion Eng. Design* **2018**, *135*, 174–182. [CrossRef]
56. Moradi, M.M.; Aval, H.J.; Jamaati, R. Effect of pre and post welding heat treatment in SiC-fortified dissimilar AA6061-AA2024 FSW butt joint. *J. Manuf. Proc.* **2017**, *30*, 97–105. [CrossRef]
57. Shibayanagi, T.; Maeda, M.; Naka, M. Microstructure and its high temperature stability in a friction stir processed 5083 aluminum alloy. *J. Jpn. Inst. Light Met.* **2006**, *56*, 347–353. [CrossRef]
58. Sato, Y.S.; Watanabe, H.; Kokawa, H. Grain growth phenomena in friction stir welded 1100 Al during post-weld heat treatment. *Sci. Technol. Weld. Join.* **2007**, *12*, 318–323. [CrossRef]
59. Kalinenko, A.; Kim, K.; Vysotskiy, I.; Zuiko, I.; Malopheyev, S.; Mironov, S.; Kaibyshev, R. Microstructure-strength relationship in friction-stir welded 6061-T6 aluminum alloy. *Mater. Sci. Eng.* **2020**, *793*, 139858. [CrossRef]
60. Baker, T.N.; Rahimi, S.; Wei, B.; He, K.; McPherson, N.A. Evolution of microstructure during double-sided friction stir welding of microalloyed steel. *Metall. Mater. Trans.* **2019**, *50*, 2748–2764. [CrossRef]
61. Kalinenko, A.; Mishin, M.; Shishov, I.; Malopheyev, S.; Zuiko, I.; Novikov, V.; Mironov, S.; Kaibyshev, R.; Semiatin, S.L. Mechanisms of abnormal grain growth in friction-stir welded aluminum alloy 6061-T6. *Mater. Char.* **2022**, *194*, 112473. [CrossRef]
62. Humphreys, F.J.; Hatherley, M. *Recrystallization and Related Phenomena*, 2nd ed.; Elsevier: Oxford, UK, 2004.